20XX-01-XXXX

Evaluating emissions in a modern compression ignition engine using multi-dimensional PDF-based stochastic simulations and statistical surrogate generation

Author, co-author (Do NOT enter this information. It will be pulled from participant tab in MyTechZone)

Affiliation (Do NOT enter this information. It will be pulled from participant tab in MyTechZone)

Abstract

Digital engineering workflows, involving physico-chemical simulation and advanced statistical algorithms, offer a robust and cost-effective methodology for model-based internal combustion engine development. In this paper, a modern Tier 4 capable Cat® C4.4 engine is modelled using a digital workflow that combines the probability density function (PDF)-based Stochastic Reactor Model (SRM) Engine Suite with the statistical Model Development Suite (MoDS). In particular, an advanced multi-zonal approach is developed and applied to simulate fuels, in-cylinder combustion and gas phase as well as particulate emissions characteristics, validated against measurements and benchmarked with respect to the predictive power and computational costs of the baseline model. The multi-zonal SRM characterises the combustion chamber on the basis of different multi-dimensional PDFs dependent upon the bulk or the thermal boundary layer in contact with the cylinder liner. In the boundary layer, turbulent mixing is significantly weaker and heat transfer to the liner alters the combustion process. The integrated digital workflow is applied to perform parameter estimation based on the in-cylinder pressure profiles and engine-out emissions (i.e. NO_x, CO, soot and unburnt hydrocarbons; uHCs) measurements. Four DoE (design-of-experiments) datasets are considered, each comprising measurements at a single load-speed point with various other operating conditions, which are then used to assess the capability of the calibrated models in mimicking the impact of the input variable space on the combustion characteristics and emissions. Both model approaches predict in-cylinder pressure profiles, NO_x, and soot emissions satisfactorily well across all four datasets. Capturing the physics of emission formation near the cylinder liner enables the multi-zonal SRM approach to provide improved predictions for intermediates, such as CO and uHCs, particularly at low load operating points. Finally, fast-response surrogates are generated using the High Dimensional Model Representation (HDMR) approach, and the associated global sensitivities of combustion metrics and emissions are also investigated.

Introduction

Model-based engineering analyses support decision and policy making processes, reduce vehicular/machine and powertrain development costs, and speed up the progression of technology readiness levels (TRL). The adoption of innovative virtual or digital engineering workflows augmented with experimental data-based analyses is increasingly important given the degree of variability and complexities of the modern powertrains and the emissions (both gas phase and particulate phase) compliance requirements.

Engine calibration, which relies on engine dynamometers and vehicle testing, offers a static tabular relationship between the engine-controlled variables and the corresponding steady-state operating points within the operating map for incorporating into the Engine Control Unit (ECU) [1], and is aimed at maintaining performance optimality and reduction of engine-out emissions. The measurement-driven calibration methodology involves the use of Design of Experiments (DoE), where the data point is processed to establish statistical response surface models for determining the variations and the measured response (i.e. engine performance, combustion characteristics, and emissions). The operation of the ECU actuators is guided by the actuator map settings from the engine calibrations, which are tuned with the help of optimisation techniques based on the responses at individual load-speed points and by interpolation for any points in-between. The poor extrapolative capabilities of purely statistical models provide the impetus to combine the advanced data-driven statistics with adequately detailed yet computationally efficient physico-chemical simulators. Furthermore, a combination of measurements data and model-based digital workflows can be then used to populate data required for formulating fast-response calibration models.

Such model-based methodologies utilising calibrated zero-dimensional (0D) or multi-dimensional models have been largely applied toward the estimation of engine performance indicators such as indicated mean effective pressure (IMEP), or combustion characteristics such as maximum in-cylinder pressure, and crank angle degrees at 50 % fuel mass fraction burnt (CA50) [2,3]. Additionally, the predictions from the fast-response 0D models are then utilised for feed-forward control applications concerning the ECU [4,5,6,7]. The accuracy of the empirical model or a fit is a vital factor to the design of searching a system optimum. Here, physics-based models not only offer higher level of accuracy, but also take into account a wide range of input variables [8]. Multi-dimensional Computational Fluid Dynamic (CFD) modelling can be applied to describe in detail the physical processes for the in-cylinder turbulent combustion and flow fields within the engine air and combustion systems. Such a 3D CFD model further supported by optimisation algorithm has been applied to populate the training datasets to construct response surfaces between design parameters and objective functions [9]. However, the 3D CFD models especially for turbulent combustion applications, remain computationally expensive and prohibit the evaluation of the whole design space (7-8 input variables) in tractable computational times. For operating an efficient and accurate model-based calibration, it is necessary to combine the predictive capability of simulation with practical computational power, so that multiple engine cycles and multiple load-speed engine operating points can be simulated. The present paper focuses on advancement and application of such an integrated digital

engineering workflow that combines adequately-detailed physico-chemical models with advanced statistical algorithms.

The physico-chemical simulator within the digital workflow is the stochastic reactor model (SRM) Engine Suite. This is then integrated with an advanced statistical toolkit, Model Development Suite (MoDS), and applied as a digital workflow to perform parameter estimation, surrogate model generation and global sensitivity analysis.

The SRM Engine Suite component of the workflow is derived from a probability density function (PDF) transport equation assuming statistical homogeneity. The PDF approach offers a way to model in-cylinder inhomogeneities in equivalence ratio Φ, and temperature T. The sub-processes in the context of an IC engine operation, such as the turbulent mixing, heat transfer to the cylinder walls, multiple direct injections, chemical kinetics, etc. are taken into account via the corresponding sub-models within the SRM Engine Suite. For variable density flows, a MDF (mass density function) transport equation is used which is solved using a Monte Carlo particle method with an operator splitting technique. Detailed derivations from first principles, parametric behaviour, and convergence studies has been published previously [10-16]. The SRM Engine Suite has been previously applied to the simulation of fuels [17, 18], various combustion operation modes such as spark ignition [19, 20], low temperature combustion [21-24] and compression ignition [25,26], as well as gas phase and particulate emissions [27-30].

MoDS has also been applied to study uncertainty propagation and parametric estimation in the context of internal combustion (IC) engines previously [31,32]. Recently, the integrated digital workflow comprising the SRM Engine Suite and MoDS has been applied to perform automated calibration based on measurements data for a C4.4 Diesel-fuelled compression ignition engine, covering the entire load-speed operating window [33]. The SRM Engine Suite was then validated against measurements data, and a reasonably good agreement was achieved between the model and experiments for in-cylinder pressure profiles, NO_x and soot emissions.

From the perspective of intermediate emissions such as CO and uHC (unburned hydrocarbons), the near-wall reactive flows have shown to play a key role in determining the thermal efficiency of combustion systems and the formation of pollutants [34]. Within the combustion chamber, large temperature variations ($\sim 400 - 800$ K) occur within a thin layer (~ 1.0 mm) next to the cylinder wall [35]. Within these turbulent boundary layers, chemical reactions cease to take place due to the enthalpy loss to the in-cylinder walls. The PDFs of scalar quantities, such as fuel mass fractions and temperature, are found to be significantly affected by the near-wall mechanism [36].

The aim of this paper is to present an extension of the SRM Engine Suite in terms of a stochastic reactor model network (termed multi-zonal SRM), in order to resolve the boundary layer and thus enhance the physical accuracy in addressing those near-wall phenomena and the ensuing formation of emissions. The integrated digital workflow containing the physico-chemical model advancements is then applied and validated against measurements performed as four sets of DoE data points within the load-speed map. The structure of this study is the following:

1. To apply the single-zonal (SRM-SZ) and multi-zonal (SRM-MZ) PDF-based stochastic reactor model to the Cat® C4.4 ACERT turbocharged Diesel-fuelled Compression Ignition (CI) engine to evaluate combustion and emissions characteristics over the four sets of DoE points.
2. To benchmark and demonstrate the benefits of the multi-zonal approach relative to the single zonal approach.
3. To formulate a fast-response HDMR surrogates to assess the global sensitivity of combustion metrics and emissions to the input variable space.

Experimental Data

The data used for model calibration and validation has been obtained from a Cat® C4.4 ACERT turbocharged Diesel-fuelled CI engine. Table 1 provides the basic engine geometry data. Four 'design-of-experiments' (DoE) datasets are studied, comprising two 'full-load, rated-speed' DoEs (1800-100 % and 2200-100 %), and one 'peak-torque' DoE (1400-100 %) on the power curve, as well as a 'part-load' condition DoE (2200-27 %); the distribution of these four points in load-speed space is shown in Figure 1. Within each dataset there are around 60 distinct measurements of in-cylinder pressure profiles and engine-out emissions, corresponding to different engine operating conditions, with variations in the intake manifold pressure, intake manifold temperature, EGR, injected fuel mass, pilot injection timing and main injection timing. Hereafter the term 'case' is used to refer to a single set of these conditions. The measurement data from the test bed are pressure and emissions (i.e. NOx, CO, uHCs and Soot). The gas phase emissions are measured in units of parts per million by volume (ppmv) with a tolerance target of 3 % and soot indicates carbon fraction with a measurement tolerance of 5 %.

Table 1 – Engine geometry for the Cat® C4.4 ACERT single-turbocharged Diesel-fuelled Compression Ignition engine.

Engine Type	4-stroke
Bore	105 mm
Stroke	127 mm
Connecting rod length	219 mm
Wrist pin offset	0.5 mm
Compression ratio	16.5

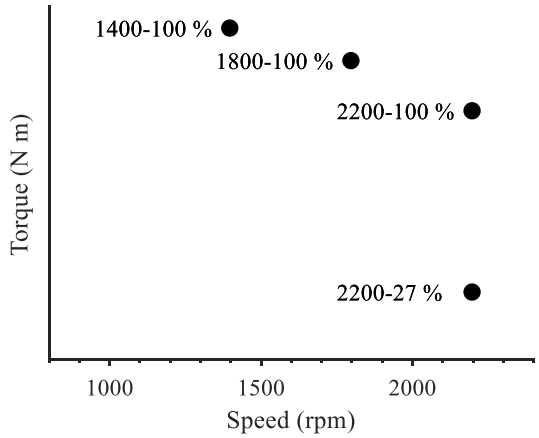

Figure 1 – The four sets of DoE data included in this analysis.

Model description

The components of the integrated workflow, i.e. the SRM Engine Suite and MoDS are explained in this section. This workflow was then applied to generate a calibrated model of a Cat C4.4 ACERT™ turbocharged Diesel-fuelled CI engine, and then to test the predictive power of the workflow using additional experimental data.

Stochastic Reactor Model (SRM)

Based on the PDF transport equation approach, the SRM calculates the progression of scalar variables, such as the mass fraction of chemical species Y_j ($j = 1, \dots, S$, where j denotes the species index and S is the total number of chemical species), and temperature T as a function of time t. The random scalar variables can be combined into a vector $\boldsymbol{\psi} = (\psi_1, \dots, \psi_S, \psi_{S+1}) = (Y_1, \dots, Y_S, T)$, and the joint composition PDF is denoted by $f(\boldsymbol{\psi}; t)$.

In order to account for density variations in the in-cylinder turbulent combustion, it is convenient to apply a MDF. The MDF is related to the PDF, and can been written as:

$$\mathcal{F}(\boldsymbol{\psi}; t) \equiv \rho(\boldsymbol{\psi}) f(\boldsymbol{\psi}; t) \tag{1}$$

The MDF transport equation for the SRM can be expressed as follows:

$$\frac{\partial}{\partial t}\mathcal{F}(\boldsymbol{\psi}; t) = \underbrace{-\sum_{j=1}^{S+1} \frac{\partial}{\partial \psi_j}\left[G_j(\boldsymbol{\psi})\mathcal{F}(\boldsymbol{\psi}; t)\right]}_{\text{chemical reaction}} + \underbrace{\sum_{j=1}^{S+1} \frac{\partial}{\partial \psi_j}\left[A(\boldsymbol{\psi})\mathcal{F}(\boldsymbol{\psi}; t)\right]}_{\text{turbulent mixing}}$$

$$\underbrace{-\frac{1}{V}\frac{dV}{dt}\mathcal{F}(\boldsymbol{\psi}; t)}_{\text{piston movement}} \underbrace{-\frac{\partial}{\partial \psi_{S+1}}\left[U(\psi_{S+1})\mathcal{F}(\boldsymbol{\psi}; t)\right]}_{\text{convective heat transfer}}$$

$$\underbrace{+\frac{\mathcal{F}_c(\boldsymbol{\psi}; t)}{\tau_{crev}} - \frac{\mathcal{F}(\boldsymbol{\psi}; t)}{\tau_{cyl}}}_{\text{crevice flow}} + \underbrace{\frac{\mathcal{F}_f(\boldsymbol{\psi}; t)}{\tau_f}}_{\text{fuel injection}} \tag{2}$$

where $G_j(\boldsymbol{\psi})$ is the chemical kinetic operator, $\mathrm{A}(\boldsymbol{\psi})$ is the turbulent mixing function, V is sweep volume, $U(\psi_{S+1})$ is the heat transfer function, $\mathcal{F}_\mathrm{c}$ and $\mathcal{F}_\mathrm{f}$ are the MDFs corresponding to the crevice flow. The characteristic residence time of in-cylinder gas, crevice gas and fuel are denoted by τ_cyl, τ_crev and τ_f. The terms on the right-hand side of Equation 2 describe the physical in-cylinder processes of chemical reactions, turbulent mixing, heat transfer, piston movement, crevice flow and fuel injection respectively.

The multi-dimensional MDF transport equation is then solved using a Monte Carlo particle method with a second-order operator splitting algorithm [16]. The initial MDF, $\mathcal{F}(\boldsymbol{\psi}; \mathrm{t})$ is approximated by a stochastic particle ensemble (discrete measures) denoted by $\mathcal{F}^N(\boldsymbol{\psi}; \mathrm{t})$.

A backward differentiation formula (BDF) of the ordinary differentiation equations (ODEs) solver is used for adaptive time stepping to control the accuracy of the chemistry solution. A third-order low storage Runge-Kutta scheme is adopted for explicit time advancement of the $k - \varepsilon$ turbulence transport equation used within the turbulent mixing sub-model which is explained next.

The turbulent mixing source term is particularly important in case of CI engine modelling, since it determines how molecular diffusion affects composition and scalar micro-mixing. In this analysis, mixing is computed using a combination of concepts originally proposed by the coalescence-dispersion (Curl) mixing model [37] and the EMST (Euclidean minimum spanning tree [38]) model. The Curl model randomly selects and mixes stochastic particle pairs towards their mean composition. However, it does not take *localness* into account; that is, nothing prevents a 'cold' particle, which might represent a fluid parcel near the cylinder liner, mixing directly with a 'hot' or reacting parcel having a higher probability to be located in the combustion chamber core. The EMST model accounts for localness by defining neighbouring particles in composition space. For an ensemble of size N, each particle has $N - 1$ neighbours (termed "edges"). The evolution of the composition vector $\boldsymbol{\psi}^{(i)}$ is given by:

$$w^{(i)}\frac{d\boldsymbol{\psi}^{(i)}}{dt} = -\alpha\Sigma_{v=1}^{N-1} 2w_v\left[\left(\boldsymbol{\psi}^{(i)} - \boldsymbol{\psi}^{(n_v)}\right)\delta_{i,m_v} + \left(\boldsymbol{\psi}^{(i)} - \boldsymbol{\psi}^{(m_v)}\right)\delta_{i,n_v}\right] \tag{3}$$

where each particle pair (m_v, n_v) is connected by the v^{th} edge, δ_{ij} is the Kronecker delta, α is the decay rate of the scalar variances, $w^{(i)}$ is the weighting of the particle index, i, and w_v is the minimum of the sum of the particle weights on either side of the edge. The hybrid model applied in this study utilises both Curl model as well as a localness mixing model based on the EMST approach to account for inhomogeneities in the charge composition.

The more detailed parameterisation is required to capture the engine flow field like swirl, tumble squish, injection etc., and it integrates these sub-models into SRM to achieve predictive capability**.** The turbulent mixing time, $\tau = C_\tau\, k/\varepsilon$, measures the rate of variations in the composition variance for each model, where C_τ is the mixing model constant, k is the turbulent kinetic energy and its dissipation rate ε. The turbulent kinetic energy k is evaluated using a quasi-dimensional turbulence modelling approach [39], which amounts to solving the $k - \varepsilon$ turbulence transport equation

$$\frac{dk}{dt} = \frac{dk_{prod}}{dt} + \frac{dk_{den}}{dt} + \frac{dk_{inj}}{dt} + \frac{dk_{squish}}{dt} - \varepsilon \tag{4}$$

where the terms on the R.H.S are production terms due to the initial tumble and swirl, density variation, injection, and squish volume respectively, and a sink term due to viscous dissipation. For a comparison between mixing times in a stochastic reactor model approach with those calculated in 3D CFD simulations, the reader is referred to Franken *et al.* [40].

A modified Woschni correlation [34] is adopted in this analysis in order to calculate the heat transfer coefficient h_g [41, 42]. It is defined as:

$$h_g = 3.26B^{-0.2}P^{0.8}T^{-0.55}w^{0.8} \tag{5}$$

where B is the cylinder bore, P is the in-cylinder pressure, T is the in-cylinder temperature and w is the average in-cylinder gas velocity. w is defined as:

$$w = C_1\bar{s}_P + C_2\frac{V_d T_r}{P_r V_r}(P - P_m) \tag{6}$$

where $\bar{s}_P$ is the mean piston speed, V_d is the displaced volume and the subscript 'r' refers to a reference state at the instant of inlet valve closure (IVC). The motored cylinder pressure is denoted by P_m and C_1 and C_2 are model parameters. Interested readers can find further details in Ref. [42].

The chemical surrogate model for the Diesel fuel [43] adopted in this study is summarised in Table 2. The surrogate mechanism has been applied to the modelling of combustion and emissions for Diesel fuelled HCCI, PPCI and CI engines [44]. The level of detail in the fuel oxidation and emissions formation pathways model is characterised by the number of species and chemical reactions. Increasing the number of species results in a more accurate solution, but at the cost of increased computational time [45].

Table 2 – Chemical model and computational time

Fuel oxidation and emissions formation model	CMCL diesel surrogate with NOx v1.2
Number of species	38
Number of reactions	50
Operating system	Windows
Processor	Intel 3GHz 8 cores
Computational time/cycle [s]	~160

The Model Development Suite (MoDS)

MoDS is a highly flexible software package designed to simplify model development using an advanced suite of numerical and statistical tools. It has been designed to couple closely with the SRM, automatically extracting the necessary data to perform (e.g.) parameter estimation based on experimental data and construct surrogates for the model outputs. Of the many algorithms available in MoDS, two in particular are used throughout this study, and are summarised below.

Sobol Sequences

Sobol sequences [46] are designed to produce points distributed in a *K*-dimensional space such that they have low *discrepancy*[*]. The resulting points are more uniformly distributed than pseudo-random points (see Figure 2), but avoid the symmetries and inefficiencies associated with points on a grid.

Figure 2 – A comparison between random and Sobol sampling with 500 points in a 2D (θ_1, θ_2) parameter space.

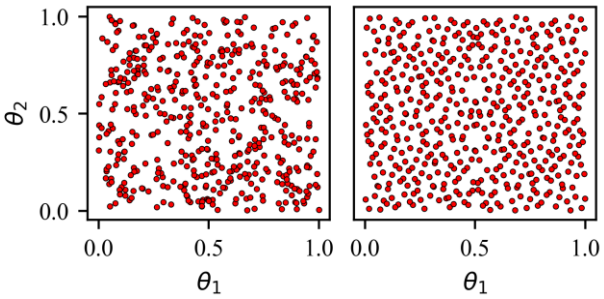

An additional advantage of Sobol sequences is that they are easily extensible; existing points do not need to be adjusted in order to maintain the low discrepancy when new points are added.

MoDS uses Sobol sequences for two main applications:

1. To make initial guesses when performing optimisation (e.g. model parameter estimation).
2. As the fitting points for surrogate models that span large-*K* input parameter spaces.

A comprehensive description of the mathematics used to generate a Sobol sequence can be found in [47]. The key elements of that work are summarised below for the reader's convenience.

The k^{th} element of the vector $\boldsymbol{\theta}$ generated from the n^{th} term of a Sobol sequence can be calculated as

$$\theta_k(n) = \sum_{l=1}^{L} e_l(n) D_l^{(k)}, \tag{7}$$

where the sum uses digit-by-digit mod-2 binary addition, $\boldsymbol{D}$ is an array of 'direction numbers' and e_l is the l^{th} digit of n in its binary representation, $n=(e_L\, e_{L-1} \ldots e_2\, e_1)$. In order to define $D_l^{(k)}$ we must first introduce the order-m_k binary difference operator, L_k:

$$L_k u_i \equiv u_{i+m_k} + a_1^{(k)} u_{i+m_k-1} + \cdots + a_{m_k-1}^{(k)} u_{i+1} + u_i = 0, \tag{8}$$

where all of the u_i and a_i belong to the field $\mathbb{Z}_2 \equiv \{0,1\}$. All of the solutions to Equation 8 are periodic; any sequence $u_0, u_1, \ldots, u_m$ will eventually repeat. The L_k which cycle over of all of the 2^m-1 possible non-trivial sequences (i.e. all except $u_i=0, \forall i$) before they repeat are called 'monocyclic'. The $D_l^{(k)}$ are generated using a set of these monocyclic operators via the equation

$$L_k D_l^{(k)} = 2^{-m_k} D_l^{(k)}, \tag{9}$$

where $D_l^{(k)}=2^{-l}$ *for* $1 \le l \le m_k$

The choice of the ***D***, and therefore ***L***, completely determines the sequence and its properties. The one-dimensional projections are guaranteed to possess a low discrepancy, but by choosing ***L*** such that the ***D*** satisfy certain further conditions, the discrepancy of the points in higher dimensional subspaces can also be minimised [48].

High Dimensional Model Representation (HDMR)

HDMR is a method for surrogate model generation that is particularly well suited to input vector spaces with a large number of dimensions. It involves the decomposition of each output into a sum of terms, each of which depend on only a subset of the inputs, that is

$$y = f(\boldsymbol{x}) = f_0 + \sum_{i=1}^{N_x} f_i(x_i) + \sum_{i=1}^{N_x} \sum_{j=i+1}^{N_x} f_{ij}(x_i, x_j) + f_{12\ldots N_x}(x_1, x_2, \ldots, x_N), \tag{10}$$

where N_x is the number of input parameters and f_0 is the mean value of $f(\boldsymbol{x})$. For most practical applications, terms involving more than two inputs make a negligible contribution [49, 50], so y can be approximated as:

$$y \approx f_0 + \sum_{i=1}^{N_x} f_i(x_i) + \sum_{i=1}^{N_x} \sum_{j=i+1}^{N_x} f_{ij}(x_i, x_j) \tag{11}$$

Whilst it is possible to evaluate each term directly using numerical integration, a more efficient method is to approximate $f_i(x_i)$ and $f_{ij}(x_i, x_j)$ using analytic functions, $\phi_k(x_i)$ [50]:

[*] Discrepancy measures the difference between the fraction of all points contained in a subspace and the fraction of the total volume occupied by that subspace [46].

$$f_i(x_i) = \sum_{k=l}^{M} \alpha_{i,k}\phi_k(x_i) \quad (12)$$

$$f_{ij}(x_i, x_j) = \sum_{k=l}^{M'} \sum_{l=k+1}^{M'} \beta_{ij,kl}\phi_k(x_i)\phi_l(x_j) \quad (13)$$

where $\boldsymbol{\phi_k(x_i)}$ are *orthonormal* functions, that is

$$\int \phi_k(x_i)dx_i = 0 \quad (14)$$

and

$$\int \phi_k(x_i)\phi_l(x_i)dx_i = \delta_{kl} \quad (15)$$

The coefficients can then be calculated as

$$\alpha_{i,k} = \int f(\boldsymbol{x})\, \phi_k(x_i)dx \quad (16)$$

$$\beta_{ij,kl} = \int f(\boldsymbol{x})\phi_k(x_i)\phi_l(x_j)dx \quad (17)$$

An added benefit of the decomposition technique described above is that the global sensitivities are straightforward to obtain. The contribution of each input, or combination of inputs, to the total variance is described by ([49])

$$\sigma_{\bar{y}}^2 = \sum_{i=1}^{N_x} \int_{-1}^{1} f_i^2(x_i)dx_i + \sum_{i=1}^{N_x} \sum_{j=i+1}^{N_x} \int_{-1}^{1}\int_{-1}^{1} f_{ij}^2(x_i, x_j)dx_i dx_j$$
$$= \sum_{i=1}^{N_x} \sigma_{\bar{y}i}^2 + \sum_{i=1}^{N_x} \sum_{j=i+1}^{N_x} \sigma_{\bar{y},ij}^2 \quad (18)$$

The sensitivities are then trivially computed by dividing by the total variance, $\boldsymbol{\sigma_{\bar{y}}^2}$.

Results and Discussion

Single-Zonal and Multi-Zonal SRM

The PDF transport equation (Equation 2) characterises the single zonal SRM (SRM-SZ), wherein N stochastic particles are used to represent the distributions of fluid parcels in the cylinder or combustion chamber. The mean quantities of the PDF are approximated by:

$$\langle \psi(t) \rangle \approx \frac{1}{N}\sum_{i=1}^{N} \psi^{(i)}(t) \quad (19)$$

A stochastic particle can be understood as a homogeneous region inside the combustion chamber containing a certain amount of mass, but without any geometrical shape or location. The stochastic particle ensemble as a whole is a discrete representation of the distribution of the composition space, from which various moments, such as means and standard deviations can be derived. The number of stochastic particles governs the precision of SRM calculations. In this study, a nonlinear statistical weighting for stochastic particles is used with a ratio of 15 between the weights of the largest and smallest particles**.** Convergence was obtained with 100 stochastic particles.

The evolution of the stochastic particles in local equivalence ratio-temperature ($\Phi - T$) space can be seen in Figure 3 for the SRM-SZ. Figure 3 (a) uses the in-cylinder pressure profile to illustrate where the four snapshots lie in the compression-expansion cycle. Note that the profile has been normalised by a reference value P_{ref}. In Figure 3 (b), each circle represents an individual stochastic particle within the cylinder. The colours of the circles encode the concentration of hydrocarbons. Greyscale contours identify regions in $\Phi - T$ space where soot and NO_x are produced. Interested readers can refer to Ref. [51] for further details. Figure 4 shows that, prior to the injection, the mixture is largely homogeneous, with $\Phi = 0.0$ and T close to the IVC temperature. After the injection, stochastic particles are spread out in the lean region ($\Phi < 1.0$) and gradually move toward the fuel-rich region ($\Phi > 1.0$) as they receive more fuel. The initial inhomogeneity generated by the injection evolves further through the combined effects of heat release due to chemical reactions and turbulent mixing. Note that the evolution of the ensemble in temperature space can be seen more clearly in the PDFs in Figure 4 (a). The most fuel-rich stochastic particles, where oxidation rates are low, are responsible for the formation of soot and unburned hydrocarbons. As the end of the expansion stroke, the temperature decreases and oxidation rates reduce further, allowing soot and hydrocarbons to survive until Exhaust Valve Opening (EVO).

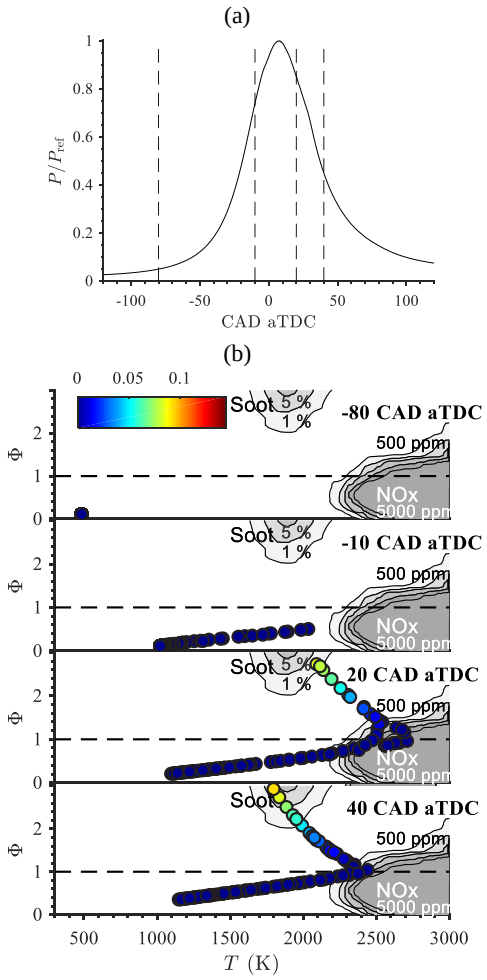

Figure 3– (a) Variation of normalised pressure P/P_ref with crank angle (CAD aTDC). Vertical broken lines indicate the time instants at CAD= -80, -10, 20 and 40 respectively. (b) Instantaneous scatter plots of the stochastic particles in Φ-T space for the SRM-SZ at four different crank angles. The colour indicates the uHC concentration, horizontal dashed lines indicate stoichiometric conditions ($\Phi = 1.0$). Greyscale contours show the regions where soot and NO_x production is expected (see Ref. [51] for numeric values).

In the present work, The SRM-MZ has been developed in order to capture the effects of near-wall, non-premixed combustion in modern diesel engines and improve the prediction of engine-out uHCs emissions. The stochastic particle ensemble is divided into two zones: the boundary and the bulk. In the boundary, a PDF is introduced to mimic the physics of the thermal boundary region (see Figure 4 (b)), and it encapsulates all walls inside the combustion chamber. The bulk

zone remains similar to the SRM-SZ, except that there is no longer any heat transfer directly to the cylinder liner: it can only exchange heat with the boundary zone. In contrast, the boundary layer is characterised by greatly diminished turbulent mixing, and a narrow distribution of temperatures, both due to the proximity of the wall. It has been demonstrated in both numerical [52] and experimental [53, 54] analyses that the zone of influence of the wall can extend to ~1 mm in the normal direction to the wall. This equates to around four per cent of the combustion chamber in the engine considered for the present study. For simplicity, and as a relatively conservative estimate, we assign one per cent of the total charge mass to the wall zone in the SRM-MZ. The importance of the boundary layer is disproportionate to its size: it mediates heat transfer to the walls and acts as a sink for species that would otherwise be oxidised. The mean temperature of the boundary layer particles (represented by the blue curve in Figure 4) is closely coupled to that of the wall, where the wall temperature is determined by experimental measurements. Since particles within the boundary tend to be of similar composition, the full localness mixing submodel is not necessary. Instead, the Curl model is employed for pair-wise mixing of mass and enthalpy between zones, with the rate of inter-zonal mixing determined as part of the model calibration.

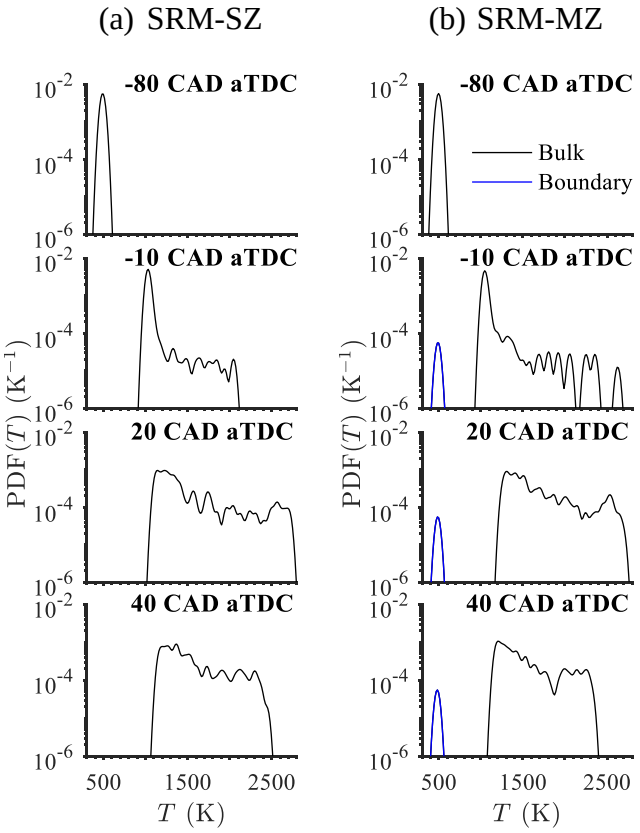

Figure 4 - The temperature PDFs in the (a) SRM-SZ and (b) SRM-MZ at four different crank angles.

In the SRM-MZ, the PDF-based injection sub-model is modified such that boundary zone stochastic particles receive liquid fuel directly from the injection pulses. A reduced evaporation rate is set for the boundary zone in order to mimic the time lag associated with injected fuel reaching the wall. Figure 5 illustrates the PDF during the injection period(s). Boundary zone particle indices start from $i = 90$, the rest of the particles lie within the bulk zone. The majority of the fuel goes into the bulk zone; however, a relatively small amount of the fuel is present in the boundary zone.

Figure 6 shows that fuel-rich particles within the boundary layer travel along the vertical direction in $\Phi - T$ space after the start of injection. The loss of enthalpy to the 'cold' walls limits combustion within the boundary zone, such that particles are not able to burn, or have large deviations in temperature due to chemical heat release. Figure 4 (b) shows that the boundary zone has a monomodal PDF, with mean temperature close to that of the wall. Significant amounts of fuel-rich mixture remain late in the engine cycle (see Figure 6), contributing to the statistics of the gas phase uHCs emission at engine-out.

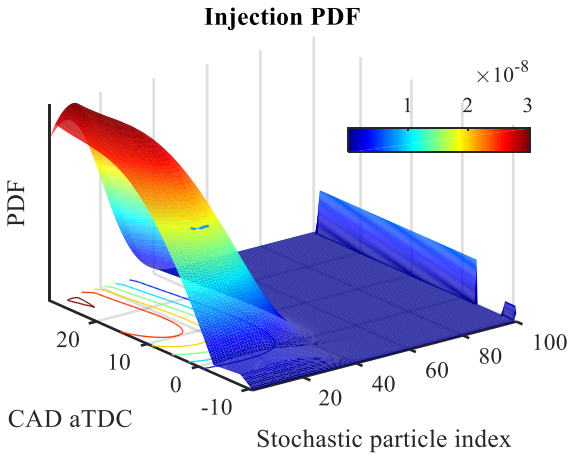

Figure 5 – The injection PDF as a function of crank angle for the SRM-MZ. The surface colour indicates the PDF magnitude.

Calibration and Validation Procedure

In order to calibrate the SRM to match the measured in-cylinder pressure profiles and emissions, MoDS was set up to estimate optimal values for a number of model inputs.

The values of those inputs calibrated for the 2200-14% DoE dataset are listed in Table 3. Parameters are divided between five categories: turbulent mixing, direct injection, heat transfer, the empirical soot model and the boundary zone (SRM-MZ only).

The turbulent mixing parameters are constants in the $k - \varepsilon$ turbulence transport equation (C_{inj}, C_{den}, C_{diss}) (see Equation 4). The direct injection parameters include:

i. a term that is directly related to the injection spray angle within the cylinder (α_{inj})
ii. the Sauter Mean Diameter constant (SMD_A) and
iii. the liquid fuel evaporation coefficient (λ_{evap}), which influences the atomisation of the spray injected into the turbulent flow.

The heat transfer model controls heat flux between the combustion chamber surface and the cylinder charge. C_1 determines the piston speed dependence in the Woschni correlation, while C_2 controls the extent to which heat transfer is modified during combustion (see Equation 6). The rates of soot formation and oxidation in the Hiroyasu-NSC empirical sub-model [55, 56] are controlled by pre-exponential multipliers (C_{sfpe} and C_{sope} respectively) and exponential multipliers (C_{sfe} and C_{soe} respectively).

For the MZ-SRM, several additional parameters were estimated:

i. The relative size of the boundary zone (λ_{MZ})
ii. The mass fraction of injected fuel that impinges on the cylinder walls (α_{Wall})
iii. A constant to control inter-zone mixing (C_{MZ}), which imply the mass and heat transfer from bulk and boundary zone.

Table 3: Parameters estimated for the 2200-14% DoE dataset.

	Parameter	SRM-SZ	SRM-MZ
Turbulent Mixing	C_{inj}	5.95	4.7
	C_{Den}	0.01	0.01
	C_{Diss}	3.76	4.0
Direct Injection	α_{inj}	875	1430
	SMD_A	6156	6719
	λ_{evap}	0.388	0.388
Heat Transfer	C_1	1.13	1.33
	C_2	0.03	0.03
Empirical Soot Model	C_{sfpe}	0.15	0.46
	C_{sope}	0.24	0.62
	C_{sfe}	3.91	7.67
	C_{soe}	0.16	0.43
Boundary Zone	λ_{MZ}	-	0.032
	α_{Wall}	-	0.034
	C_{MZ}	-	0.41

The full set of input values were calibrated independently for each of the four DoE datasets, with 18 randomly selected cases included in the calibration each time, equating to approximately 30 per cent of the available data. The best parameters were estimated by minimising the *objective function*, defined by:

$$\phi(\boldsymbol{\theta}) = \sum_i^N \left(\frac{y_i - f(\boldsymbol{x_i}, \boldsymbol{\theta})}{\sigma_i}\right)^2 \quad (20)$$

Where y_i is the experimentally measured value of output i, σ_i is the measurement uncertainty, x_i is the vector of process conditions associated with the measurement and θ is the vector of model parameters.

Each MoDS run consisted of the following stages:

1. Coarsely sample the input parameters space by evaluating the SRM at $2^{N_{input}+1}$ Sobol points.
2. Use the Sobol point with the lowest objective function to set the initial values of θ.
3. Perform a local optimisation using the Hooke and Jeeves algorithm [57] in order to minimise $\phi(\theta)$.

While MoDS provides several other choices of optimisation algorithm, including gradient-based methods, Hooke and Jeeves was selected due to its superior performance when applied to similar problems in the past [33].

Having calibrated the SRM for the 18 randomly selected cases, the input values are then frozen (independently for each DoE dataset) and the model is evaluated for the remaining cases (40-45 depending on the dataset). This validation procedure provides a way to gauge the predictive capacity of the model.

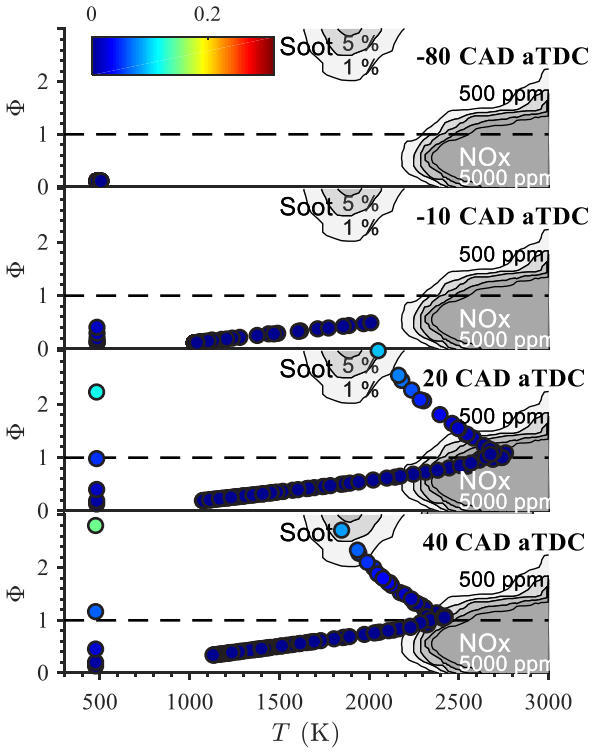

Figure 6 – Instantaneous scatter plots of the stochastic particles in Φ-T space for the SRM-MZ at four different crank angles. The colour indicates the uHC concentration, horizontal dashed lines indicate stoichiometric conditions (Φ=1.0). Greyscale contours show the regions where soot and NO_x production is expected (see Ref. [51] for numeric values).

Calibration Results

Figure 7 and Figure 8 show in-cylinder pressure profiles, apparent heat release rate and emissions for each DoE dataset, comparing the calibrated SRM-SZ and SRM-MZ with experimental data. In each case, only the 18 sets of process conditions used to calibrate the models are considered. While an excellent agreement between the measured and simulated pressure profiles is obtained, only marginal differences are observed between the single and multi-zonal approaches.

Figure 8 shows the concentrations of NO_x (i.e. $NO + NO_2$), CO, uHCs, and soot measured from the C4.4 engine versus those predicted by the SRM-SZ and SRM-MZ. In each panel, both experiment and model values are normalised by the maximum experimental value. Points where the model evaluations match the experimental data exactly would lie on the diagonal dashed line. The calibrated SRM-SZ and SRM-MZ are both able to match the measured NO_x concentrations for all four DoEs; with the vast majority of cases consistent within experimental uncertainty. While the SRM-SZ gives a satisfactory match to the CO and uHCs data, the SRM-MZ improves results for all four DoEs, most notably at low load (2200-27%), where the scatter about the 1:1 line is substantially reduced. These results are driven by the modelling of the thermal boundary layer in the SRM-MZ: retaining fuel-rich parcels near the wall gives rise to a wider possible range of CO and uHCs concentrations, meaning higher values can be matched without degrading the agreement for lower values. Over all four datasets, the most challenging data for the models to reproduce are the most extreme values of soot, and to a lesser extent, CO.

Figure 7 – Comparison between the pressure (solid lines) and apparent heat release rate (dash lines) profiles from measurements and from the calibrated SRM-SZ and SRM-MZ. A single representative case was selected for each of the four DoE datasets; the full set of profiles can be found in the appendix (Figure A1). Note that both pressure and heat release rate values have been divided by a fixed reference value.

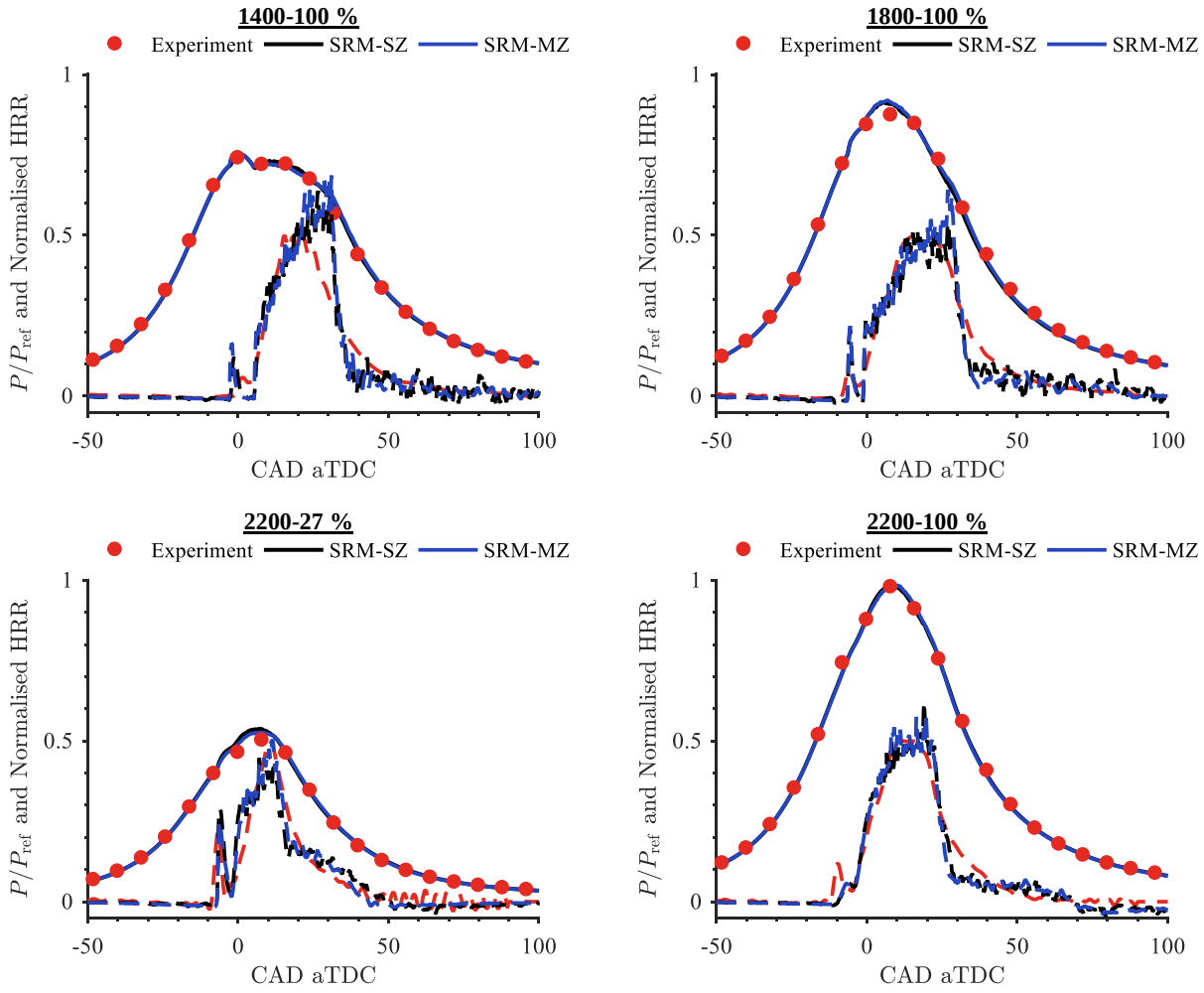

Validation Results

This section presents the results of applying the calibrated SRM-SZ and SRM-MZ to those DoE cases that were not included in the calibration: around 40 cases for each dataset. As such, it is a clean test of the predictive capability of the models. For the sake of brevity, in-cylinder pressure profiles are not plotted here, but we note that the degree of agreement with the experimental data is similar to that seen in Figure 9. The capacity of the calibrated SRM-SZ to predict in-cylinder pressure has also been previously demonstrated in Figure 19 of [33].

Validation results for CO, NOx, soot and uHCs can be seen in Figure . Both models predict the measured NOx concentrations satisfactorily well. The SRM-SZ shows a small systematic overprediction for both full-load, rated-speed DoEs, although we note that the magnitude of the discrepancy is comparable to the uncertainty in the experimental data. For other emissions, the pattern is similar to that seen in the calibrated cases. For uHCs, the multi-zonal approach provides more accurate predictions across all four DoES, but particularly at higher torque (1400-100% and 1800-100%). The performance of the two models for CO is similar, although there are a small number of cases for which the SRM-SZ overpredicts the measured value by a factor of 1.5-2. For soot, both models perform well for the majority of cases, but fail to predict the highest values seen in the data.

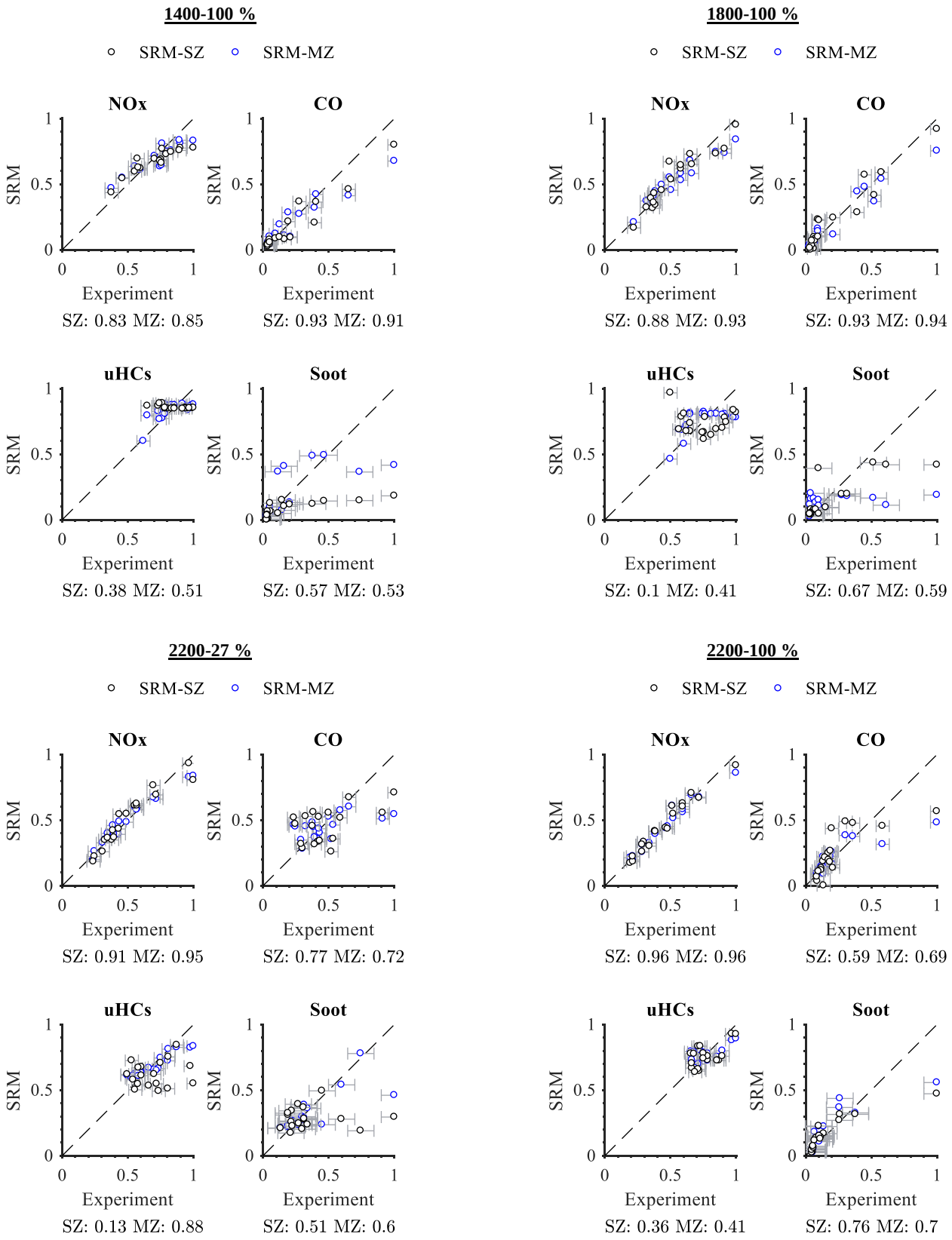

Figure 8 – Gas and particulate phase emissions for the 18 randomly selected sets of operating conditions used to calibrate the SRM-SZ and SRM-MZ to each of the four DoE datasets. Values are normalised by the maximum experimental value for each emission. The dashed line indicates a 1:1 relation. The correlation coefficient, R^2, is listed for the SZ and MZ below each plot.

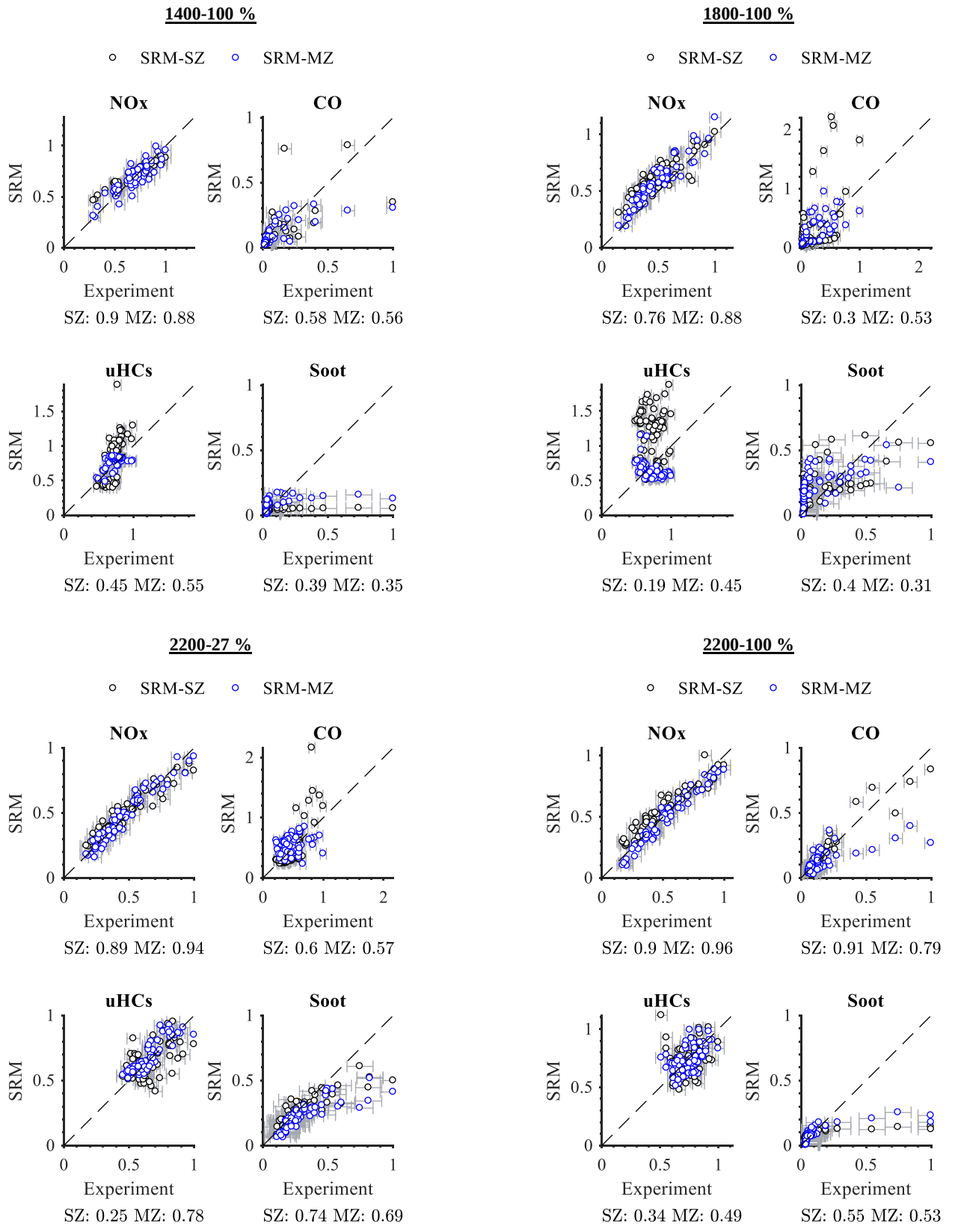

Figure 9 – Gas and particulate phase emissions for the ~40 sets of operating conditions used to validate the SRM-SZ and SRM-MZ for each of the four DoE datasets. Values are normalised by the maximum experimental value for each emission. The correlation coefficient, R^2, is listed for the SZ and MZ below each plot.

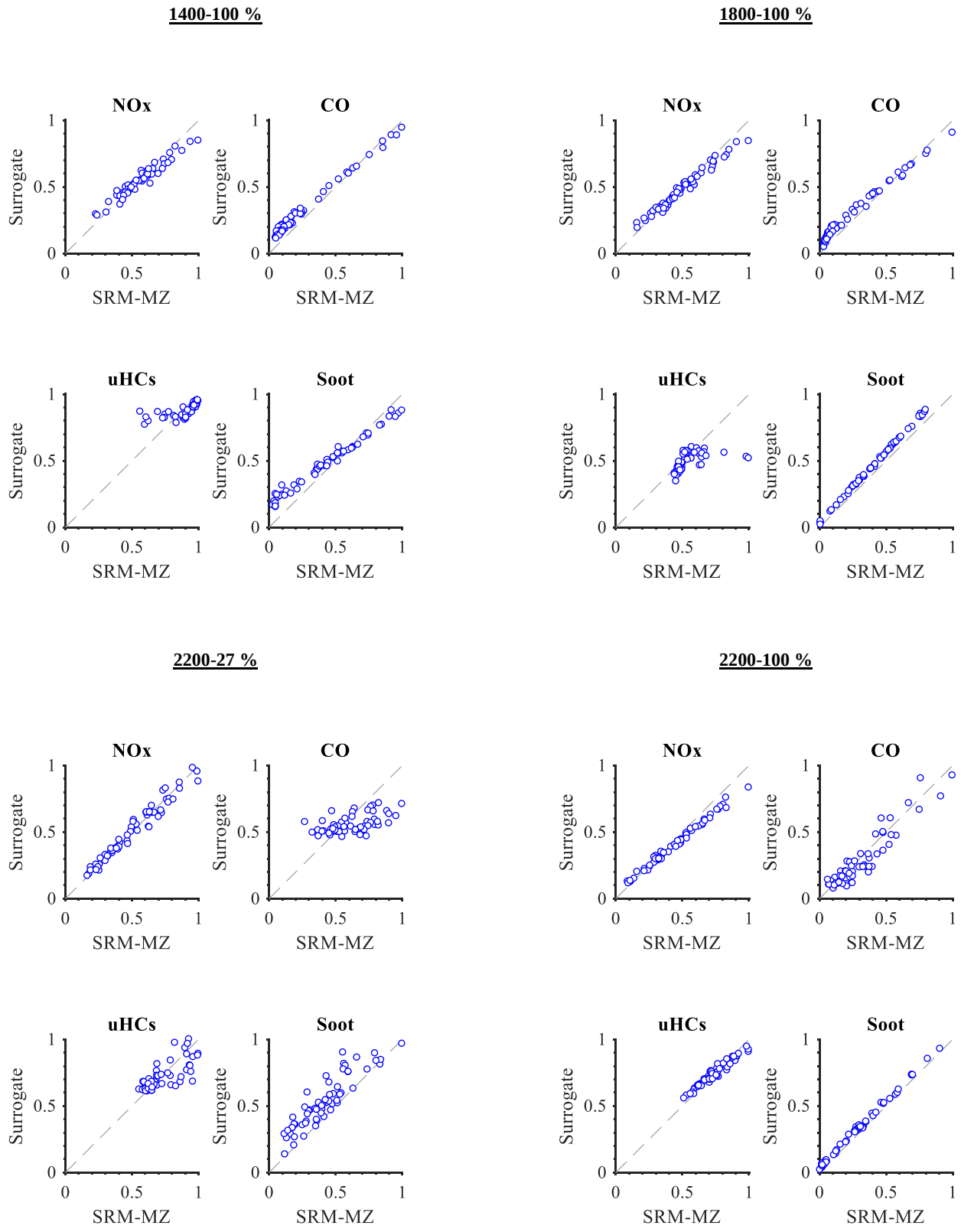

Figure 10 – Comparison between the gas and particulate phase emissions predicted by the SRM-MZ and by HDMR surrogates fitted to each output. Values are normalised by the maximum SRM-MZ value for each emission.

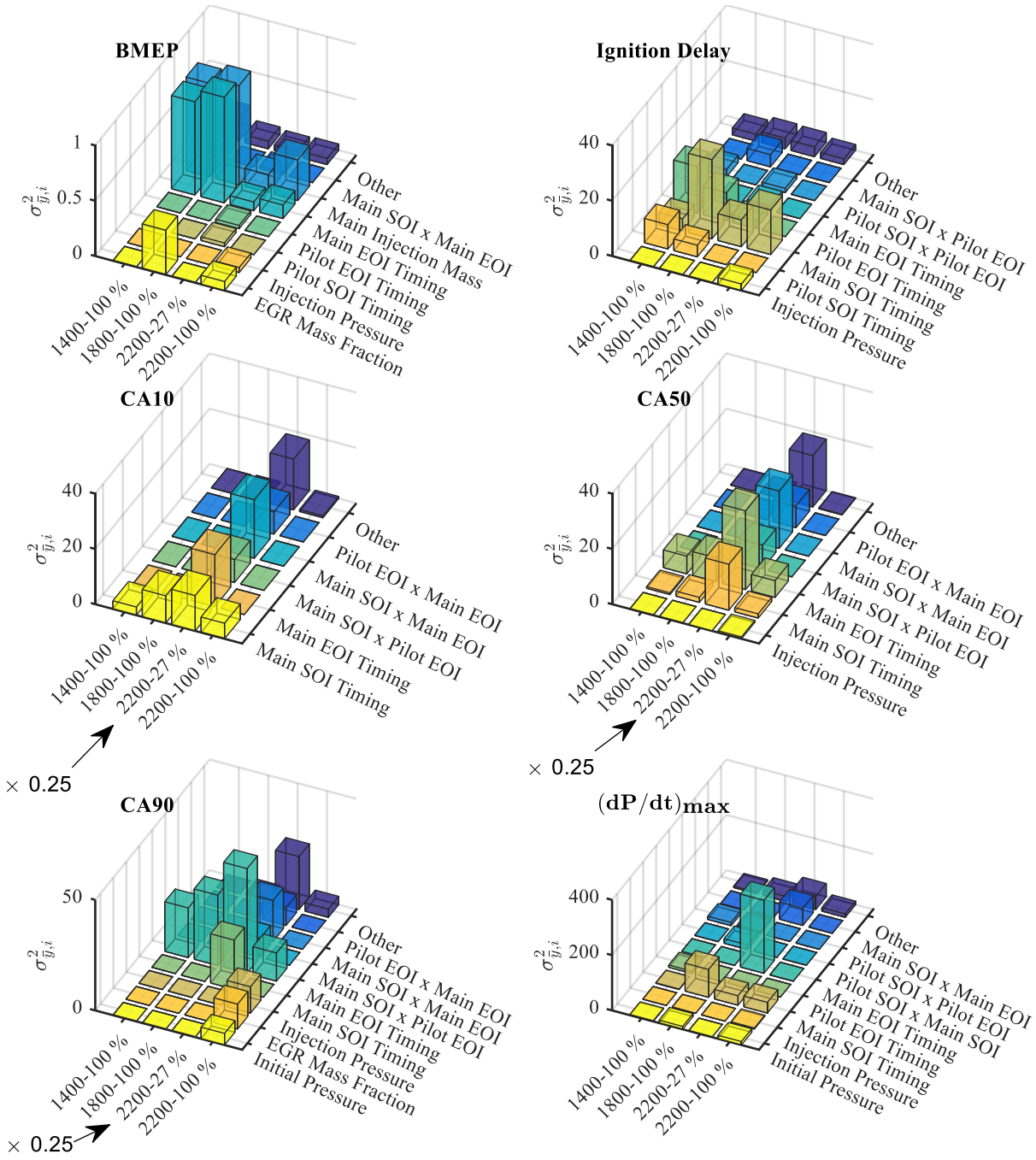

Figure 11 – Contributions to the variance in several combustion metrics for all four DoE datasets. Terms contributing less than five per cent of the total variance are grouped together in the "Other" category. Arrows indicate instances where the variances have been scaled in order to reveal trends and details in other datasets.

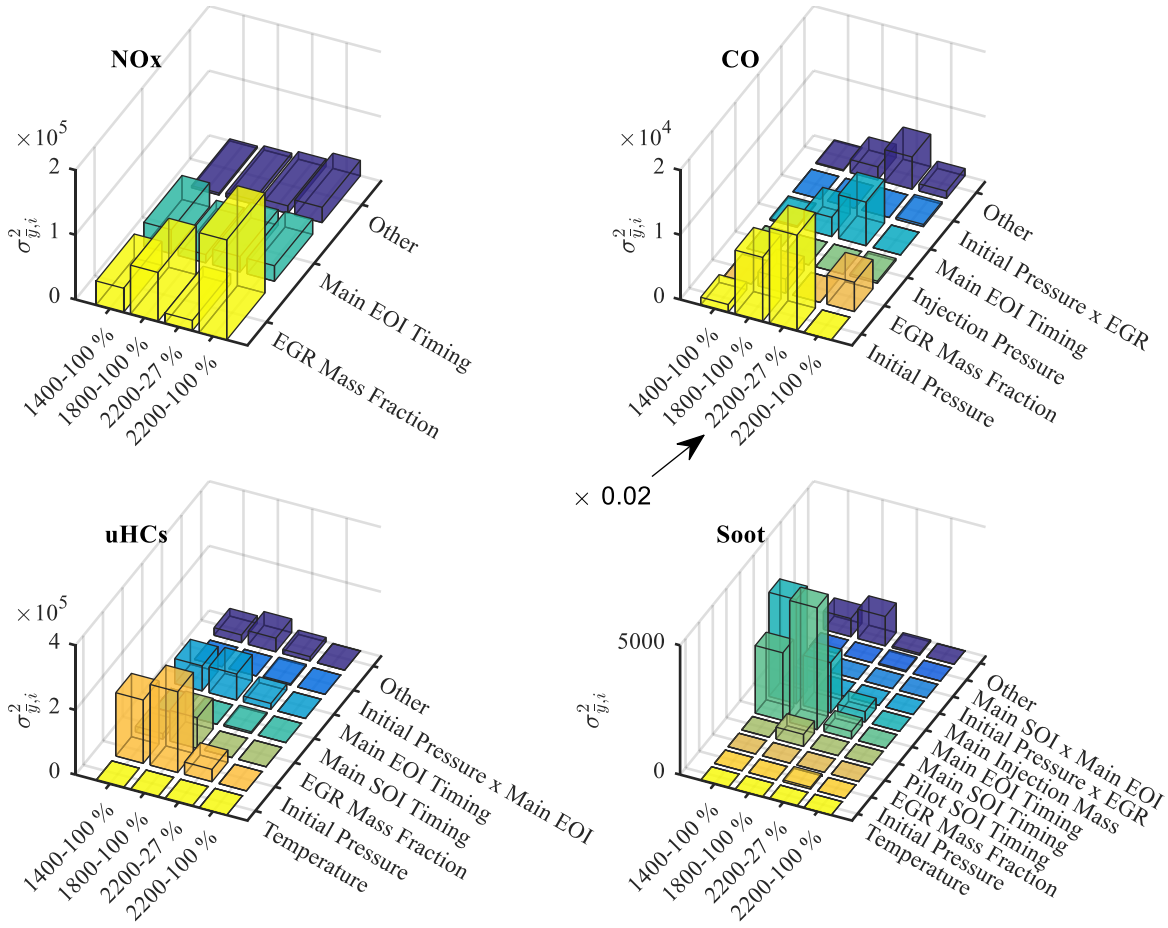

Figure 12 – Contributions to the variance in each emissions output for all four DoE datasets. Terms contributing less than five per cent of the total variance are grouped together in the "Other" category. Arrows indicate instances where the variances have been scaled in order to reveal trends and details in other datasets.

Surrogate and Sensitivity Analysis

As discussed in previous sections, the generation of surrogate models using the HDMR method automatically yields the variance of each surrogate output to every (combination of) models input(s). In practice, surrogates were constructed by evaluating the SRM at $2^{Ninput+1}$=1024 Sobol points and determining the coefficient values using Equations 16 and 17. One surrogate was generated for each of the SRM emissions outputs and each point on the in-cylinder pressure profile, as well as for a number of combustion metrics: the crank angle at which ten, fifty and ninety per cent of heat release is complete (CA10,CA50,CA90) the brake mean effective pressure (BMEP), the maximum in-cylinder pressure (P_{max}), the maximum rate of pressure change $(dP/dt)_{max}$, and the ignition delay. Due to its superior performance in predicting CO and uHCs, the multi-zonal SRM was used as the basis for all surrogates considered in this section.

In order to determine the sensitivity of the model to different inputs, and by extension, the influence of different operating conditions on real-world engine performance and emissions, it is important to test and ensure that the surrogates provide an accurate approximation to the detailed model. To verify the quality of the generated surrogates, these were evaluated at the input values (operating conditions) corresponding to each experimental case and directly compared to output from the SRM. Figure 10 plots model versus surrogate for CO, NO_x, soot and uHCs for each DoE dataset. In general, the surrogates capture the model behaviour effectively. The biggest discrepancies are seen in CO at part load and in the uHCs, though even in those cases differences are typically less than 20 per cent. These results give a degree of reassurance that sources of significant variance in the surrogate are also influential in the physical model, and therefore are important for real-world applications.

To assess the influence of different operating conditions, the absolute variances due to the most significant inputs, or combination of inputs, are plotted in Figure 11 and Figure 12, for combustion characteristics and emissions respectively. Each column corresponds to one of the DoE datasets and each category on the z-axis to an input/input combination. All terms that contribute less than five per cent in total are grouped into the “Other” category. Note that category names of the form *A x B* indicate the effects of varying inputs *A* and *B* at the same time. For several outputs, the part-load DoE has intrinsically more variance than the other DoEs, so is scaled down in order not to obscure interesting trends in the other datasets (indicated by arrows).

Many of the panels in Figure 11 support results that one might have guessed intuitively. For instance, for CA10, the start of the main injection (main SOI) is a substantial and often dominant contributor to the total variance. Cross terms associated with the pilot and main injection timings also contribute. For CA50, the end point of the main injection (main EOI) plays a more significant role, as well as the injection pressure. As one might expect, CA90 in general shows much less dependence on the main SOI but is influenced by other

parameters that effect the burn rate, such as the initial pressure, injection pressure and EGR fraction.

For all four DoEs, the BMEP variance is largely controlled by the mass of the main fuel injection event. Several terms involving the injection timings are also significant, particularly the combination of main SOI and main EOI, which can be interpreted as the injection duration.

The capacity of EGR to reduce NO_x emissions has been known for several decades [58, 59], so it is perhaps unsurprising that the SRM shows a strong link between the two. The only other significant input is the main SOI, which is the largest source of variance in the part load DoE. For both CO and uHCs, the initial pressure tends to be the most important input; injection pressure, EGR and the main injection timings also contribute. Soot is found to have the most complex set of dependencies, with typically at least six terms in the HDMR decomposition accounting for more than five per cent of the variance. Typically, the most important input variables are the main SOI, EOI and fuel mass. We note that the two high-speed DoEs (2200-27%,2200-100%) show much less soot variation overall, a trend that is also seen in the uHCs concentration.

Summary and Conclusions

An automated model calibration workflow, has been demonstrated and applied to predict in-cylinder pressure and engine-out emissions for a Cat C4.4 ACERT turbocharged Diesel-fuelled Compression Ignition (CI) engine. The workflow combines a new multi-zonal variant of the SRM with an advanced statistical toolkit, MoDS. The performance of SRM-MZ has been analysed in terms of the calibration quality and validation (predictive) results, comparing directly to the fiducial single zonal model. Both the SRM-SZ and SRM-MZ match the experimentally measured pressure profiles, NO_x and soot emissions well. In addition to this, the SRM-MZ gives more accurate predictions of uHCs, and to a lesser extent, CO. This improvement is driven by the inclusion of a boundary layer zone PDF, which provides a better description of the physics/causal relationship of near-wall emissions formation.

Finally, the statistical toolkit was used to generate HDMR surrogates for engine-out emissions and a number of combustion characteristics. The variances derived as part of the surrogate construction process were compared in order to examine the influence of different operating conditions on each of the model outputs, and by extension, on measurable quantities in the physical engine.

In addition to the analysis of the four datasets in this study, further investigation will be necessary to ensure that the SRM-MoDS calibration workflow produces robust results across the entire engine operating map.

References

1. E. Rask, E. and M. Sellanu. Simulation-based engine calibration: Tools, techniques and applications. *SAE Technical Paper 2004-01-1264*, 2004.
2. R. Mobasheri, Z. Peng Z., and S. M. Mirsalim. Analysis the effect of advanced injection strategies on engine performance and pollutant emissions in a heavy duty DI-diesel engine by CFD modeling. *International Journal of Heat and Fluid Flow*, 33:59-69, 2012.
3. M. F. Benedett, S. Berrone, and S. Scialo. Efficient combustion parameter prediction and performance optimization for a diesel engine with a low throughput combustion model. *Energy Conversion and Management*, 96:105-114, 2015.
4. R. Finesso, E. Spessa, and Y. Yang. Fast estimation of combustion metrics in DI diesel engines for control-oriented applications. *Energy Conversion and Management*, 112:254-273, 2016.
5. J. Chung, S. Oh, K. Min, and M. Sunwoo. Real-time combustion parameter estimation algorithm for light-duty diesel engines using in-cylinder pressure measurement. *Applied Thermal Engineering*, 60:33-43, 2013.
6. A. E. Catania, R. Finesso, and E. Spessa. Predictive zero-dimensional combustion model for DI diesel engine feed-forward control. *Energy Conversion and Management*, 52:3159-3175, 2011.
7. R. Isermann and H. Sequenz. Model-based development of combustion engine control and optimal calibration for driving cycles: general procedure and application. *IFAC Proceedings Volumes*, 49(11):633-640, 2016.
8. H. Sahara, Y. Kakuda, S. Kim, D. Shimo, K. Maruyana, S. Moringa, T. Hashimoto, H. Hayashibara, and M. Tetsuno. Development of model-based combustion control to ensure robustness of emissions, fuel consumption and noise performances in new generation diesel engine. *IFAC Proceedings Volumes*, 46(21):95-100, 2013.
9. Y. Shi, H. W. Ge, and R. D. Reitz. Computational optimisation of internal combustion engines. Springer, 2011.
10. M. Kraft. Stochastic Modeling of Turbulent Reacting Flow in Chemical Engineering. *Nummer 391 in Fortschrittsberichte des VDI*, Reihe 6. VDI Verlag, 1998.
11. M. Kraft, P. Maigaard, F. Mauss, M. Christensen, and B. Johansson. Investigation of combustion emissions in a homogeneous charge compression injection engine: Measurements and a new computational model. *Proceedings of the Combustion Institute*, 28(1):1195-1201, 2000.
12. M. Balthasar, F. Mauss, A. Knobel, and M. Kraft. Detailed Modeling of soot formation in a partially stirred plug flow reactor. *Combustion and Flame*, 128(4):395-409, 2002.
13. P. Maigaard, F. Mauss, and M. Kraft. Homogeneous charge compression ignition engine: A simulation study on the effects of inhomogeneities. *Journal of engineering for gas turbines and power*, 125(2):466-471, 2003.
14. A. Bhave, M. Balthasar, M. Kraft, and F. Mauss. Analysis of a natural gas fuelled homogeneous charge compression ignition engine with exhaust gas recirculation using a stochastic reactor model. *The International Journal of Engine Research*, 5(1):93-104, 2004.
15. A. Bhave and M. Kraft. Partially stirred reactor model: analytical solutions and numerical convergence study of a PDF/Monte Carlo Method. *SIAM J. Sci. Comput.*, 25(1):1798-1823, 2004.
16. A. Bhave, M. Kraft, L. Montorsi, and F. Mauss. Sources of CO emissions in an HCCI engine: A numerical analysis. *Combustion and Flame*, 144:634-637, 2006.
17. J. E. Etheridge, S. Mosbach, M. Kraft, H. Wu, and N. Collings. A Detailed Chemistry Simulation of the SI-HCCI Transition. *SAE International Journal of Fuels and Lubricants* 3(1):230-240, 2010.
18. N. Morgan, A. Smallbone, A. Bhave, M. Kraft, R. Cracknell, and G. Kalghatgi. Mapping surrogate gasoline compositions into RON/MON space. *Combustion and Flame*, 157(6):1122-1131, 2010.
19. B. Wang, S. Mosbach, S. Schmutzhard, S. Shuai, Y. Huang, and M. Kraft. Modelling soot formation from wall films in a gasoline direct injection engine using a detailed population balance model. *Applied Energy*, 163:154-166, 2016.

20. H. Wu, N. Collings, J. E. Etheridge, S. Mosbach, and M. Kraft. Spark ignition to homogeneous charge compression ignition mode transition study: a new modelling approach. *The International Journal of Engine Research*, 13:1-25, 2012.
21. S. Mosbach, H. Su, M. Kraft, A. Bhave, F. Mauss, Z. Wang, and J. X. Wang. Dual injection homogeneous charge compression ignition engine simulation using a stochastic reactor model. *International Journal of Engine Research*, 8(1):41-50, 2007.
22. J. E. Etheridge, S. Mosbach, M. Kraft, H. Wu, and N. Collings, N. A Detailed Chemistry Multi-cycle Simulation of a Gasoline Fueled HCCI Engine Operated with NVO. *SAE International Journal of Fuels and Lubricants*, 2(1):13-27, 2009.
23. L. Cao, H. Su, S. Mosbach, A. Bhave, M. Kraft, A. Dries, and R. M. McDavis. Influence of Injection Timing and Piston Bowl Geometry on PCCI Combustion and Emissions. *SAE Int. J. Engines* 2(1):1019-1033, 2009.
24. S. Mosbach, A. M. Aldawood, and M. Kraft. Real-Time Evaluation of a Detailed Chemistry HCCI Engine Model Using a Tabulation Technique. *Combustion Science and Technology*, 180(7):1263-1277, 2008.
25. A. Smallbone, A. Bhave, M. Hillman, A. Saville, R. McDavid. Virtual Performance and Emissions Mapping for Diesel Engine Design Optimisation. *SAE Technical Paper 2013-01-0308*, 2013.
26. A. Smallbone, A. Bhave, A. R. Coble, S. Mosbach, M. Kraft, and R. M. McDavid. Identifying Optimal Operating Points in term of Engineering Constraints and Regulated Emissions in Modern Diesel Engines. *SAE Technical Paper 2011-01-1388*, 2011.
27. A. J. Smallbone, A. R. Coble, A. Bhave, S. Mosbach, M. Kraft, N. Morgan, and G. Kalghatgi. Simulating PM emissions and combustion stability in gasoline/Diesel fuelled engines, *SAE Technical Paper 2011-01-1184*, 2011.
28. S. Mosbach, M. S. Celnik, A. Raj, M. Kraft, H. R. Zhang, S. Kubo, and K. O. Kim. Towards a detailed soot model for internal combustion engines. *Combustion and Flame*, 156(6):1156-1165, 2009.
29. J. E. Etheridge, S. Mosbach, M. Kraft, H. Wu, and N. Collings. Modelling soot formation in a DISI engine. *Proceedings of the Combustion Institute*, 33:3159-3167, 2011.
30. D. Kittelson and M. Kraft. Particle Formation and Models. *Encyclopedia of Automotive Engineering*, 1-23, 2015.
31. G. Brownbridge, A. Smallbone, W. Phadungsukanan, M. Kraft, and B. Johansson. Automated IC engine model development with uncertainty propagation. *SAE Technical Paper 2011-01-0237*, 2011.
32. G. Brownbridge, S. Mosbach, M. Kraft, A. Smallbone, A. Coble, and A. Bhave. Automated parameterization of conventional 1D cycle simulation tools with advanced parametric and experimental uncertainty propagation. *IAV DoE Conference*, Berlin, Germany, 2011.
33. O. Parry, J. Dizy, V. Page, A. Bhave, and D. Ooi. Fast response surrogates and sensitivity analysis based on physico-chemical engine simulation applied to modern compression ignition engines. *IAV*, 2017.
34. J. B. Heywood. Internal Combustion Engine Fundamentals. 1st Edition, McGraw Hills, 1998.
35. A. Gruber, J. H. Chen, D. Valiev, and C. K. Law. Direct numerical simulation of premixed flame boundary layer flashback in turbulent channel flow. *J. Fluid Mech.*, 709:516-542, 2012.
36. J. Lai and N. Chakraborty. Effects of Lewis number on head on quenching of turbulent premixed flames: A direct numerical simulation analysis. *Flow Turb. Combust.*, 96(2):279-308, 2016.
37. R. L. Curl. Dispersed phase mixing: I. Theory and effects in simple reactors. *AIChE journal*, 9(2):175-181, 1963
38. S. Subramaniam, S. B. Pope. A mixing model for turbulent reactive flows based on Euclidean minimum spanning trees. *Combustion and Flame*, 115(4):487-514, 1998.
39. S. Grasreiner, J. Neumann, C. Luttermann, M. Wensing, and C. Hasse. A quasi-dimensional model of turbulence and global charge motion for spark ignition engines with fully variable valvetrains. *International Journal of Engine Research*, 15(7):805-816, 2014.
40. T. Franken, A. Sommerhoff, W. Willems, A. Matrisciano, H. Lehtiniemi, A. Borg, A. and F. Mauss, Advanced Predictive Diesel Combustion Simulation Using Turbulence Model and Stochastic Reactor Model. *SAE Technical Paper 2017-01-0516*, 2017.
41. A. Smallbone, K. M. Banton, A. Bhave, J. Akroyd, M. Hillman, R. C. R. Riehl, and N. M. Morgan. Meeting the challenges associated with low-carbon alternative fuels through advanced CAE technologies. *Internal Combustion Engines: Performance, Fuel Economy and Emissions*, 137, 2014.
42. G. Bernard, M. Scaife, A. Bhave, D. Ooi, and J. Dizy. Application of the SRM engine suite over the entire load-speed operation of a US EPA tier 4 capable IC engine. *SAE Technical Paper 2016-01-0571*, 2016.
43. A. Smallbone, A. Bhave, A. R. Coble, S. Mosbach, M. Kraft, and R. McDavid. Identifying optimal operating points in terms of engineering constraints and regulated emissions in modern diesel engines. *SAE Technical Paper 2011-01-1388*, 2011.
44. A. R. Coble, A. Smallbone, A. Bhave, S. Mosbach, M. Kraft, P. Niven, and S. Amphlett. Implementing detailed chemistry and in-cylinder stratification into 0/1-D IC engine cycle simulation tools. *SAE Technical Paper 2011-01-0849*, 2011.
45. J. Etheridge, A. Bhave, S. Smallbone, A. Coble, S. Mosbach, and M. Kraft. Optimisation of injection strategy, combustion characteristics and emissions for IC engines using advanced simulation technologies. *SAE Technical Paper 2011-26-0080*, 2011.
46. I. M. Sobol'. On the distribution of points in a cube and the approximate evaluation of integrals. *USSR Computational Mathematics and Mathematical Physics*, 86-112, 1967.
47. I. M. Sobol'. On the Systematic Search in a Hypercube. *SIAM Journal on Numerical Analysis*, 790-793, 1979
48. I. M. Sobol'. Uniformly distributed sequences with an additional uniform property. *USSR Computational Mathematics and Mathematical Physics*, 16(5), 236-242, 1976.
49. H. Rabitz and O. F. Aliş. General foundations of high-dimensional model representations. *Journal Of Mathematical Chemistry*, 25(2):197-233, 1999.
50. G. Li, S. Wang, and H. Rabitz. Practical Approaches To Construct RS-HDMR Component Functions. *The Journal of Physical Chemistry A*, 106(37):8721-8733, 2002.
51. T. Kamimoto and M. Bae. High combustion temperature for the reduction of particulate in diesel engines. *SAE Technical Paper 1988-04-23*, 1988.
52. T. J. Poinsot, D. C. Haworth, and G. Bruneaux. Direct simulation and modeling of flame-wall interaction for premixed turbulent combustion. *Combustion and Flame*. *95*(1-2):118-132, 1993.
53. W. M. Huang, R. Greif, and R. S. Vosen. The effects of pressure and temperature on heat transfer during flame quenching. *SAE Transactions*, 96:548–558, 1987.
54. C. K. Westbrook, A. A. Adamchzuk, and G. A. Lavoie. A numerical study of Laminar flame wall quenching. *Comb. Flame*, 40:81–99, 1981.
55. H. Hiroyasu, T. Kadota, and M. Arai. Development and use of a spray combustion modeling to predict diesel engine efficiency and pollutant emissions: Part 1 combustion modeling. *Bulletin of JSME*, 26(214): 569-575, 1983.
56. J. R. Walls and R. F. Strickland-Constable. Oxidation of carbon between 1000–2400 C. *Carbon* 1(3):333-338, 1964.

57. R. Hooke and T. A. Jeeves. Direct Search" Solution of Numerical and Statistical Problems", *Journal of the ACM*, 8(2):212-229, 1961.
58. R. D. Kopa and H. Kimura. Exhaust Gas Recirculation as a Method of Nitrogen Oxides Control in an Internal Combustion Engine. *APCA 53rd Annual Meeting*, Cincinnati, Ohio, 1960.
59. S. Y. Yee and W. Linville. The Effect of Exhaust Gas Recirculation on Oxides of Nitrogen. *ACPA 53rd Annual Meeting*, Cincinnati, Ohio, 1960.

Contact Information

Dr Jiawei Lai

CMCL Innovations

Sheraton House

Castle Park, Cambridge CB3 0AX, UK

Email: jlai@cmclinnovations.com

Acknowledgments

This work was supported by the Advanced Propulsion Centre UK in the framework of the APC3 Project 113059 -ASCENT (Advanced Systems for Carbon Emission reduction through New Technology).

Definitions/Abbreviations

aTDC	At top dead centre
BMEP	Brake Mean Effective Pressure
CAD	Crank Angle Degree
CFD	Computational Fluid Dynamics
CI	Compression Ignition
DoE	Design of Experiment
ECU	Engine Control Unit
EGR	Exhaust Gas Recirculation
EMST	Euclidian Minimum Spanning Tree
EVO	Exhaust Valve Opening
HCCI	Homogeneous Charge Compression Ignition
HDMR	High Dimensional Model Representation
IMEP	Indicated Mean Effective Pressure
IVC	Inlet Valve Closure
MDF	Mass Density Function
MoDS	Model Development Suite
PDF	Probability Density Function
PPCI	Partially Premixed Compression Ignition
SOI	Start of Injection
EOI	End of Injection
SRM	Stochastic Reactor Model
TRL	Technology Readiness Levels
uHC	Unburned Hydrocarbons

Appendix

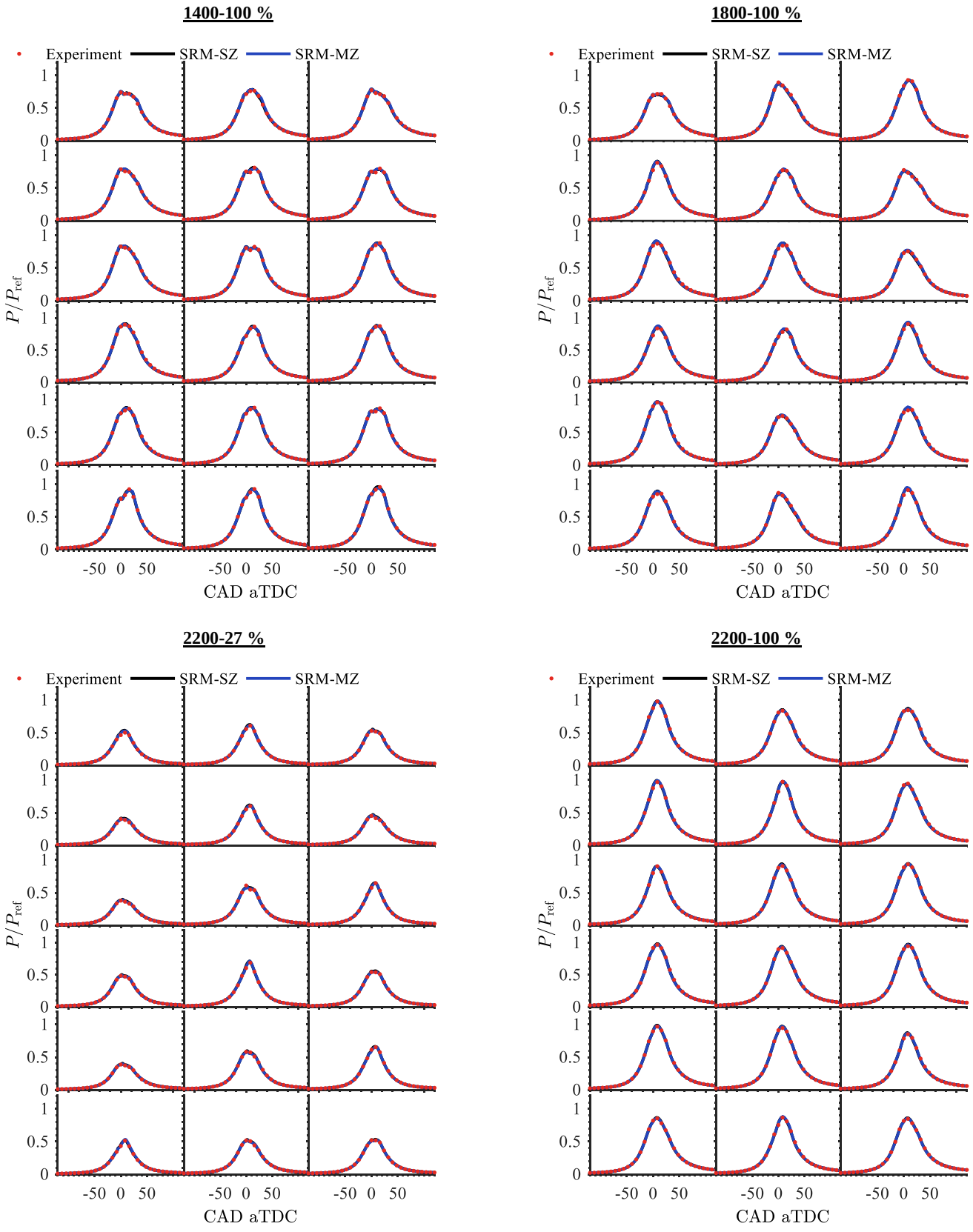

Figure A1 - Pressure profiles for each of the 18 randomly selected sets of operating conditions used to calibrate the SRM-SZ and SRM-MZ for the four DoE datasets. Pressure values have been normalised by a fixed reference pressure P_{ref}.